IEEE Robotics and Automation Letters (RA-L) paper, presented at ICRA 2026, Vienna, Austria. Cite as RA-L paper.

A teleoperated control for robot-aided percutaneous surgery: an application to needle insertion in nephrolithotomy

Clemente Lauretti[1], Rosaura Morfino[1], Francesco Cocco[1], Francesco Prata[2], Rocco Papalia[2] and Loredana Zollo[1]

***Abstract*—Minimally Invasive Percutaneous Surgery (MIPS) has revolutionized medical practice by allowing access to internal organs through needle puncture, thus avoiding large incisions. Tele-operated robotic systems address MIPS challenges, but current literature lacks real-time needle path re-planning during surgery, which is crucial due to organ shifts between pre-operative imaging and the intra-operative setting. Moreover, no studies have systematically compared the performance of different control strategies. This letter aims to enhance MIPS effectiveness by improving patient safety while considering efficiency, usability, and acceptability. A new tele-operated control strategy, adaptable to surgeon preferences, is introduced with application to nephrolithotomy. The strategy integrates position control for access point re-planning and two operation modes for needle advancement: OM1 – parallel position/velocity, and OM2 – master-slave position error-based. Experimental validation involved six subjects performing nephrolithotomy on a synthetic anatomical model. Results showed comparable puncture time, usability, and acceptability between modes. OM1 achieved higher needle orientation accuracy ($max\ DNA = 0.006 \pm 0.003\ [rad]$) and motion smoothness ($SM = 0.13 \pm 0.08$), while OM2 was more responsive in terms of needle displacement accuracy ($CRE = 0.8 \pm 0.9\ [mm]$). Six experts further evaluated the system, finding both modes intuitive with moderate mental and physical workload.**

***Index Terms*—Surgical Robotics: Steerable Catheters/Needles, Telerobotics and Teleoperation, Medical Robots and Systems**

I. INTRODUCTION

MINIMALLY Invasive Percutaneous Surgery (MIPS) is a surgical technique that accesses internal organs or structures through needle punctures, avoiding large incisions. Image guidance, such as computed tomography (CT), magnetic resonance (MRI), and ultrasound (US), ensures precise needle placement and real-time monitoring [1]. MIPS reduces tissue damage, bleeding, pain, and recovery time compared to open surgery. It is increasingly used for both diagnostic and therapeutic procedures, including biopsies, cancer treatments, spinal, urological, and neurosurgical interventions. MIPS has been progressively adopted in various surgical procedures for diagnostic and therapeutic purposes, including tissue biopsy, cancer treatments, spinal surgery, urology, and neurosurgery.

Despite the improvements brought by imaging techniques that provide a clearer view of the surgical scenario, percutaneous surgery remains complex and highly reliant on the surgeon's skills and experience. Indeed, the surgeon relies on kinesthetic feedback from the needle during the procedure and must have good hand-eye coordination to operate successfully [2]. Moreover, there are inherent challenges such as imaging limitations, tissue deformation, and needle deviations that further complicate the procedure. It is also important to note that the use of imaging technologies, such as CT, results in prolonged exposure of the surgeon to ionizing radiation, which over time can lead to potential health risks [3]. US, while advantageous for visualizing soft tissues, has limitations if the structures are located deep or occluded by bone. On the other hand, MR can generate detailed images of internal organs and tissues; however, it can be time-consuming and expensive, and the confined space of the MR machine may induce discomfort or anxiety in some patients.

To address these issues, many robotic systems have been proposed for percutaneous needle-based procedures. Compared to conventional methods, robotic systems offer several benefits. They provide higher accuracy in both localizing the anomaly and performing the puncture, reduce or eliminate radiation exposure, and minimize the risk of complications [4]. An analysis of the literature revealed several robotic systems designed for MIPS, each offering different levels of assistance: autonomous, cooperative, and tele-operated systems.

Among *autonomous systems*, some studies propose impedance and admittance control strategies to compensate for respiratory movements during biopsy procedures [5]. Other works [6] presented US-guided needle insertion robotic system for percutaneous puncture or CT-guided robotic [7]. Although these systems eliminate or reduce exposure to ionizing radiation for the surgeon, they do not allow direct surgeon control over the procedure. The unmodeled aspects of the surgical environment make a fully autonomous system a potential risk to the patient, highlighting the role of the surgeon's expertise in managing complications and unforeseen scenarios [8].*Cooperative systems* [9] automatically align the needle with the target area using imaging techniques, while the surgeon manually advances it. The robotic device presented in [10] aligns the needle guide with the planned trajectory under CT guidance, after manual pre-positioning. Although these systems provide

Manuscript received: July, 10, 2025; Revised August, 29, 2025; Accepted August, 29, 2025.

This paper was recommended for publication by Editor Burgner-Kahrs Jessica upon evaluation of the Associate Editor and Reviewers' comments.

This work was supported in part by the UCBM University Strategic Projects 2023 with the Prof of Concept (PoC) project BONE - Sistema robotico cooperativo per chirurgia spinale, and in part by the Piano Nazionale Ripresa e Resilienza (PNRR) - HEAL ITALIA Extended Partnership - SPOKE 2 Cascade Call - "Intelligent Health" with the project BISTOURY - 3D-guided roBotIc Surgery based on advanced navigaTiOn systems and aUgmented viRtual realitY (CUP: J33C22002920006).

[1]C. Lauretti, R. Morfino, F. Cocco and L. Zollo are with the Unit of Advanced Robotics and Human-Centred Technologies (CREO lab), Università Campus Bio-Medico, Via Alvaro del Portillo 21, Rome, 00128, Italy.

[2]F. Prata and R. Papalia are with the Department of Urology, Fondazione Policlinico Universitario Campus Bio-Medico, Via Alvaro del Portillo, 200, Roma, 00128, Italy and with the Research Unit of Urology, Department of Medicine and Surgery, Università Campus Bio-Medico di Roma, Via Alvaro del Portillo, 21, Roma, 00128, Italy

Corresponding author(s). E-mail(s): c.lauretti@unicampus.it

©2026 IEEE

IEEE Robotics and Automation Letters (RA-L) paper, presented at ICRA 2026, Vienna, Austria. Cite as RA-L paper.

control of the procedure by the surgeon, they still expose surgeons to radiation, as in conventional surgery. This issue is addressed by *teleoperated control architectures*, that combine direct surgeon control over the procedure with the elimination of radiation exposure and enhanced surgeon dexterity through motion scaling, enabling precise manipulation from a console outside the operating room. These architectures employ unidirectional or bidirectional communication between master and slave devices [11]. In bidirectional systems, the master sends position or velocity commands while receiving position, velocity, and force feedback from the slave. Position-based controls transmit scaled master movements as position references, providing high intuitiveness when workspaces are similar. However, significant size differences require substantial scaling, reducing position resolution and increasing slave velocities. To address this issue, velocity-based controls can be employed, converting master movements into velocity commands for the slave robot. An example of system implementing this control modality is the one proposed in [12] for flexible needle insertion under US guidance, which provides kinesthetic and vibrotactile feedback.

However, to the best of the authors' knowledge, the tele-operated systems proposed in the literature do not allow the surgeon to safely re-plan the needle path in real-time during the surgery by guaranteeing the appropriate distance of the robot from the patient's skin. The absence of this capability poses substantial challenges in clinical practice, where the dynamic nature of surgical procedures commonly requires trajectory adjustments due to anatomical shifts, patient positioning changes, or unforeseen conditions not evident in pre-operative imaging. These factors are recognized as common causes of inaccuracy in percutaneous procedures [13]. Moreover, there are no studies that compare the overall performance of velocity and position control modalities in robot-aided needle insertion. Identifying the optimal control mode based on control strategy performance and surgeon preference can significantly enhance patient safety during surgery, improve post-operative recovery, and increase the adoption of robots in clinical settings.

Therefore, the objective of this work is to overcome the aforementioned limitations exhibited by literature approaches by proposing a *tele-operated control architecture* for minimally invasive percutaneous surgery that allows surgeons to **safely re-plan** the needle path in real-time during intervention and is adaptable to the surgeon's use preferences. Additionally, this work addresses the current lack of **objective comparison** between different tele-operated control modes for MIPS.

The main steps of robot-aided MIPS, using the proposed control strategy, are illustrated in Fig. 1 and detailed in Sect. II-A. This work focuses on Intra-Operative Phase 1 (IOP 1) and phase 2 (IOP 2). For IOP 1 (detailed in Sect. II-B1), a motion planner generates trajectories, managed by position control, for safe real-time re-planning of the access point. Needle movements are constrained along a cylindrical surface with radius adjustable within a safe range from the patient's skin. For IOP 2 (detailed in Sect. II-B2), involving needle advancement along the puncture axis, two Operation Modes (OM) are proposed: *OM1 - parallel position/velocity mode* and *OM2 - master-slave Position Error Based (PEB) mode*, selectable according to operator preference. During both phases, intra-operative imaging techniques are essential to provide the surgeon with continuous anatomical structure visualization.

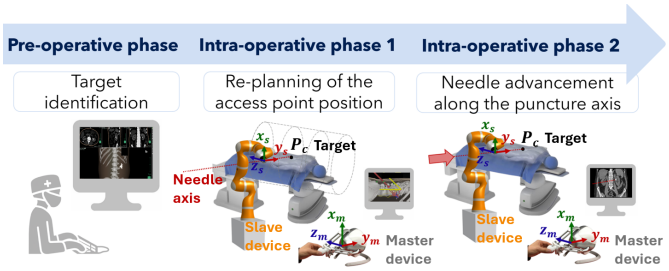

Fig. 1: Main steps of the proposed robot-aided MIPS approach.

The proposed control architecture was applied to needle insertion in percutaneous nephrolithotomy, a procedure where a needle is advanced into the renal cavities, followed by guide insertion, tract dilation, and stone removal. This surgery was selected due to its high complication rate of 20.5% with image-guided techniques, as reported in a study of 5800 cases [14]. Robotic assistance may improve success rates, reduce the number and duration of punctures, and offer a simpler learning curve compared to conventional image-guided approaches [15]. Studies have also shown that kidney position significantly changes between the supine position used for pre-operative CT and the prone position adopted during surgery [16]. Pronation reduces the skin-to-calyx distance, with variations related to sex and BMI [17]. This highlights the need for intraoperative replanning to account for anatomical shifts.

A comparative analysis of operation modes OM1 and OM2 was performed using the Novint Falcon as the master device and the KUKA LWR 4+ as the slave. Six non-expert subjects executed nephrolithotomy tasks on a synthetic anatomical model with tissue-like gelatin layers. Performance was assessed through quantitative indices evaluating procedure effectiveness (puncture accuracy), efficiency (trajectory quality and insertion time) [18], and usability. Additionally, six expert users evaluated the system in terms of intuitiveness and overall acceptability of both operation modes.

II. MATERIALS AND METHODS

A. Steps of robot-aided percutaneous surgery

As depicted in Fig. 1, a typical surgical intervention of robot-aided MIPS includes the following steps:

- Target identification (**pre-operative phase**): this step involves using pre-operative imaging data to reconstruct a 3D model of the area of interest. The goal is to locate the precise position of the target and identify the anatomical regions that need to be avoided during the puncture. Consequently, the optimal trajectory for the needle insertion can be established.
- Planning of the access point position (**IOP1**): at this stage, the surgeon can decide whether to maintain the pre-planned trajectory or modify it based on real-time feedback from the vision system. Adjustments may be necessary depending on the actual location of the organs during the intra-operative

IEEE Robotics and Automation Letters (RA-L) paper, presented at ICRA 2026, Vienna, Austria. Cite as RA-L paper.

phase. In such a scenario, through the implementation of a *motion planner* and a *position control* (see Sect. II-B1 for details), the surgeon can manipulate the master device to change the access point while maintaining an orientation such that the needle is aligned with the target.

- Needle advancement along the puncture axis (**IOP2**): once the optimal trajectory of the new access point is defined, the surgeon can use one of the two operation modes, *OM1 - parallel position/velocity* (see Sect. II-B2a for details) or *OM2 - master-slave PEB mode* (see Sect. II-B2b for details), to guide the needle to the target with real-time visual feedback. The robotic system ensures alignment with the desired axis and provides mechanical guidance to the surgeon.

B. The proposed tele-operated control architecture for robot-aided percutaneous surgery

Once the pre-operative plan has been determined (pre-operative phase), the surgeon can decide at the time of surgery, based on real-time feedback from the vision system, whether to re-plan the needle access point. At this stage (IOP1), the robot is in free space, and it is crucial to ensure that the access point can be changed while maintaining the needle orientation toward the target. Allowing the robot, and hence the needle, to move freely in the space can pose a significant risk to patient safety. To mitigate this risk, movement constraints were introduced to keep the needle at a safe distance from the patient's skin throughout this phase. For this purpose, the robot was constrained to move along a cylindrical surface, positioned at an adjustable safety distance from the patient. Operator commands, transmitted via the haptic interface, are transformed by a cylindrical Cartesian planner into cylindrical coordinate references, while an orientation planner ensures that the needle maintains its orientation relative to the target. These references are then sent to a position control in the operational space, that ensures the execution of planned trajectories. The resulting cylindrical workspace of the robot (Fig.1), demonstrates how these planners work together to maintain the correct orientation and positioning of the needle relative to the target. Subsequently, the surgeon can advance the needle (IOP2) using one of the two operation modes, i.e. OM1 - parallel position/velocity mode and OM2 - master-slave PEB mode. In both modes, the haptic interface restricts movement to the puncture axis, enhancing surgeon confidence and control intuitiveness. The difference between the two operation modes lies in how needle advancement along the puncture axis is managed. In the case of OM1, the position command supplied by the surgeon on the master device is translated into a velocity command, enabling constant speed needle insertion. Conversely, in OM2, the position command supplied by the surgeon on the master results in a change in the position of the slave, to which the needle is connected. More details on the motion planner and control laws implemented for the described phases are provided in the following sections. Furthermore, the master-side control and the slave-side controls of the proposed approach are shown in Fig. 2a and Fig. 3, respectively.

1) IOP 1 - Access point planning: The surgeon-robot configuration during the operation is illustrated in Fig. 1. The end-effector frame is denoted as $[\boldsymbol{x_s}, \boldsymbol{y_s}, \boldsymbol{z_s}]$, where the axis $\boldsymbol{y_s}$ was chosen as the puncture axis, meaning that it always points to the target. Therefore, the workspace of the robot can be represented by a cylindrical surface described by the radial direction $\boldsymbol{y_s}$ and the axial direction $\boldsymbol{z_s}$. The haptic interface frame is denoted as $[\boldsymbol{x_m}, \boldsymbol{y_m}, \boldsymbol{z_m}]$, where the $\boldsymbol{x_m}$ and $\boldsymbol{z_m}$ directions serve as the angular and linear references θ_x and Δz respectively. In particular, θ_x indicates the angle that the needle has to travel along the surface of the circumference obtained by sectioning the cylindrical surface along the $\boldsymbol{z_s}$ axis, while Δz indicates the displacement along this axis. The cylindrical surface corresponds to the workspace of the robot, which can be modified by the surgeon in real-time through

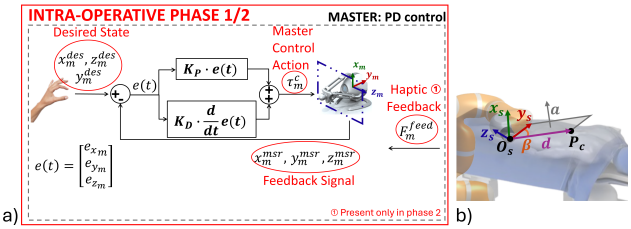

Fig. 2: a) Block diagram of master-side control, b) overview of the terms involved in the orientation planner.

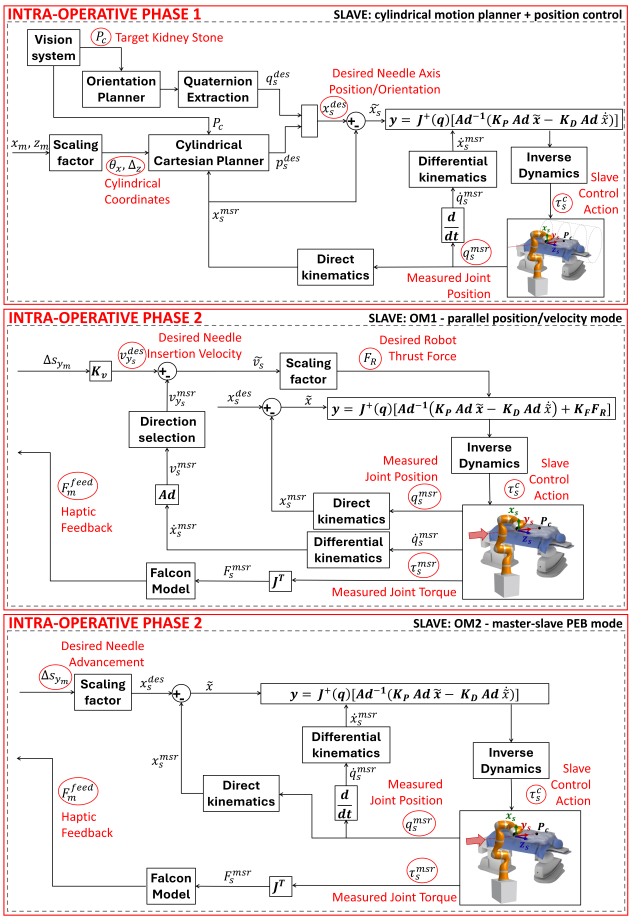

Fig. 3: Block diagram of slave-side controls.

IEEE Robotics and Automation Letters (RA-L) paper, presented at ICRA 2026, Vienna, Austria. Cite as RA-L paper.

multiplication by a scaling factor. This allows the workspace to be expanded or reduced by changing the ratio between $\boldsymbol{x_m}$ and θ_x, and between $\boldsymbol{z_m}$ and $\boldsymbol{z_s}$.

Given that haptic interfaces generally operate within a workspace of several tens of centimeters, matching small displacements with large angles could cause the manipulator to reach extremely high speeds, potentially leading to instability and compromising movement accuracy. To solve this issue, a small value for the master-slave scaling factor is chosen, and when the haptic interface approaches the boundaries of its workspace, the operator can reposition it to the center by backtracking in the opposite direction of the intended movement. This action, achieved by holding down one of the buttons on the interface handle, interrupts the stream of commands to the slave robot. Furthermore, throughout this phase, the surgeon can only move the haptic interface in the frontal plane, i.e., in the $\boldsymbol{x_m z_m} - plane$, which prevents the needle from moving along the axis $\boldsymbol{y_s}$. To ensure that the velocity of needle movement along the circumference remains controlled and does not exceed a threshold value (set at $0.005\ [m/s]$), the implemented planner re-plans whenever this limit is reached by constraining the maximum velocity.

Thus, given the desired θ_x and Δz, a cylindrical Cartesian planner based on parametric path primitives [19] was used to implement the desired motion using the parametric equations of a cylinder. Following the parametric representation $p = f(\sigma)$, where σ defines the motion direction, the planner employs the equations $x = r\cos(\theta_x)$, $y = r\sin(\theta_x)$, and $z = \Delta z$, where r is the cylinder radius and θ_x is the angle around the z-axis. In parallel, an orientation planner maintains the needle oriented towards the kidney stone, as shown in Fig. 3. The terms involved in the latter are shown in Fig.2b. Identified with $\boldsymbol{P_c}$ the target point, the vector equal to the difference between the origin of the slave frame and the target to be reached can be defined as $\boldsymbol{d} = \boldsymbol{P_c} - \boldsymbol{O_s}$. The goal is to ensure that $\boldsymbol{y_s}$ is aligned with the vector $\boldsymbol{d}$ at each instant. One possible approach to reach this objective is to define a rotation of the frame relative to the end-effector about a specific axis with a certain angle. The rotation axis $\boldsymbol{a}$ is identified by the axis orthogonal to the plane identified by $\boldsymbol{d}$ and to $\boldsymbol{y_s}$, and the corresponding angle of rotation β around this axis is equal to the angle between them. Hence, defined the rotation axis as $\boldsymbol{a} = \boldsymbol{d} \times \boldsymbol{y_s}$ and the angle of rotation as $\beta = \arccos(\boldsymbol{d} \cdot \boldsymbol{y_s})$, the relative rotation matrix $\boldsymbol{R}_{\text{rel}}$ can be expressed as

$$\boldsymbol{R}_{\text{rel}} = \begin{pmatrix} a_x^2(1-c\beta)+c\beta & a_x a_y(1-c\beta)-a_z\sin\beta & a_x a_z(1-c\beta)+a_y\sin\beta \\ a_x a_y(1-c\beta)+a_z\sin\beta & a_y^2(1-c\beta)+c\beta & a_y a_z(1-c\beta)-a_x\sin\beta \\ a_x a_z(1-c\beta)-a_y\sin\beta & a_y a_z(1-c\beta)+a_x\sin\beta & a_z^2(1-c\beta)+c\beta \end{pmatrix} \quad (1)$$

Once reported $\boldsymbol{R}_{\text{rel}}$ in the robot base frame $[\boldsymbol{x_b}, \boldsymbol{y_b}, \boldsymbol{z_b}]$ through premultiplication by the current rotation matrix $\boldsymbol{R_b^s}$, which expresses the orientation of the end-effector with respect to the robot base frame ($\boldsymbol{R} = \boldsymbol{R_b^s}\ \boldsymbol{R}_{\text{rel}}$), a synthetic representation of the orientation can be extracted through a unit quaternion $q = [\mu, \epsilon_x, \epsilon_y, \epsilon_z]$. In this way, references are created at each new desired position of the access point to ensure the needle points toward the target area.

The master-side and slave-side controls implemented during phase 1 are depicted in Fig. 2a and Fig. 3, respectively. A Proportional-Derivative (PD) controller is used to minimize the master position error $\boldsymbol{e(t)}$, given by the difference between the desired and real position, enabling the master device to accurately follow the surgeon's commands along the $\boldsymbol{x_m}$ and $\boldsymbol{z_m}$ directions. To prevent motion along $\boldsymbol{y_m}$, its desired input is set to zero. Concurrently, the corresponding gain matrices $\boldsymbol{K_P}$ and $\boldsymbol{K_D}$ are adjusted to ensure a rigid interface along this direction. On the other hand, the slave device employs a position control in the operational space to adhere to the trajectories planned through the motion planner.

The proposed position control can be derived from a conventional inverse dynamics control [20] described as follows

$$\boldsymbol{\tau_c} = \widehat{\boldsymbol{B}}(\boldsymbol{q})\ \boldsymbol{y} + \widehat{\boldsymbol{C}}(\boldsymbol{q}, \dot{\boldsymbol{q}})\ + \widehat{\boldsymbol{g}}(\boldsymbol{q}) \quad (2)$$

where $\widehat{\boldsymbol{B}}(\boldsymbol{q})$ is the estimated inertia matrix of the robot, $\widehat{\boldsymbol{C}}(\boldsymbol{q}, \dot{\boldsymbol{q}})$ is the estimated Coriolis and centrifugal terms matrix, $\widehat{\boldsymbol{g}}(\boldsymbol{q})$ is an estimate of the gravity contribution, $\boldsymbol{q}$ and $\dot{\boldsymbol{q}}$ denote the position and angular velocity of the robot joints, respectively, and $\boldsymbol{y}$ represents the stabilizing action.

The stabilizing action $\boldsymbol{y}$ is expressed as follows

$$\boldsymbol{y} = \boldsymbol{J_A^\dagger}(\boldsymbol{q}) \left[\boldsymbol{Ad^{-1}}\ (\boldsymbol{K_P}\ \boldsymbol{Ad}\ \tilde{\boldsymbol{x}} - \boldsymbol{K_D}\ \boldsymbol{Ad}\ \dot{\tilde{\boldsymbol{x}}}) \right] \quad (3)$$

where $\boldsymbol{J_A^\dagger}$ is the right pseudo-inverse of the robot analytical Jacobian, $\boldsymbol{Ad}$ is an adjoint matrix used to transform the pose error $\tilde{\boldsymbol{x}}$ from the base frame of the robot $[\boldsymbol{x_b}, \boldsymbol{y_b}, \boldsymbol{z_b}]$ to the end-effector frame $[\boldsymbol{x_s}, \boldsymbol{y_s}, \boldsymbol{z_s}]$ and is expressed as

$$\boldsymbol{Ad} = \begin{bmatrix} \boldsymbol{R_s^b} & \hat{\boldsymbol{p}}_{\boldsymbol{s}} \boldsymbol{R_s^b} \\ \boldsymbol{O}_{(3\times3)} & \boldsymbol{R_s^b} \end{bmatrix}^T \quad (4)$$

where $\boldsymbol{R_s^b}$ represents the rotation matrix that defines the orientation of the end-effector frame in relation to the base frame and $\hat{\boldsymbol{p}}_{\boldsymbol{s}}$ is the skew-symmetric matrix of the Cartesian position of the end-effector $\boldsymbol{p_s}$. The pose error $\tilde{\boldsymbol{x}}$ includes the orientation error ε_{dm}, which can be defined in terms of the Euler parameters relative to the mutual orientation between the desired and the measured orientation of the needle $\{\eta_{\text{dm}}, \varepsilon_{\text{dm}}^{\boldsymbol{e}}\}$ and is expressed as $\varepsilon_{\text{dm}} = \boldsymbol{R_s^B} \varepsilon_{\text{dm}}^{\boldsymbol{e}}$. Last, $\boldsymbol{K_D}$ and $\boldsymbol{K_P}$ are the position control gains, defined as 6x6 positive-definite diagonal matrices, which have been experimentally optimized based on empirical performance evaluation. The choice of these gains as positive-definite, together with the invertibility of the adjoint matrix, implies that the corresponding gains expressed in the base frame, $\boldsymbol{K_P^b} = \boldsymbol{A_d}^{-1} \boldsymbol{K_P} \boldsymbol{A_d}$ and $\boldsymbol{K_D^b} = \boldsymbol{A_d}^{-1} \boldsymbol{K_D} \boldsymbol{A_d}$, are also positive-definite. This follows from the fact that a congruence transformation of a positive-definite matrix, i.e., $\boldsymbol{B}^\top \boldsymbol{A} \boldsymbol{B}$ with $\boldsymbol{A} \succ 0$ and $\boldsymbol{B}$ invertible, preserves positive definiteness. Assuming that the Jacobian is not affected by singularities or redundancy, and considering that the stabilizing action $\boldsymbol{y}$ in (3) leads to a linear second-order error dynamics, this condition is sufficient to guarantee the asymptotic convergence of the position error to zero [19].

2) IOP 2 - Needle advancement along the puncture axis:

a) OM1 - Parallel Position/Velocity Mode: Once the access point and the respective orientation of the needle are established, needle insertion can proceed. At this stage, it is essential to both maintain the desired orientation/position of the needle and allow controlled movement of the needle along the puncture axis to maximize patient safety during

IEEE Robotics and Automation Letters (RA-L) paper, presented at ICRA 2026, Vienna, Austria. Cite as RA-L paper.

the procedure. The master-side control remains the same as previously presented, i.e., the PD control illustrated in Fig. 2a, with some variations explained below, while the slave-side control is shown in Fig. 3. Compared with IOP1, in this case, the desired inputs of the PD controller are set equal to zero along the $\boldsymbol{x_m}$ and $\boldsymbol{z_m}$ axes, with their respective gain matrices $\boldsymbol{K_P}$ and $\boldsymbol{K_D}$ defined to achieve high stiffness along these axes. The surgeon applies a force F_m along the $\boldsymbol{y_m}$ axis, resulting in a displacement Δs_{y_m}. This displacement is then multiplied by a factor K_v to derive a desired velocity along the puncture axis. Subsequently, through an additional scaling factor, this velocity command along the puncture axis is transformed into a thrust force F_R that the robot has to apply in order to ensure that the needle moves with the desired velocity. The described part pertains to the velocity control. Simultaneously, there is a position control acting on the $\boldsymbol{x_s}$ and $\boldsymbol{z_s}$ axes to maintain the desired puncture position/orientation. In this case, the proportional and derivative gain matrices are defined as $\boldsymbol{K_P} = diag\{k_{P_1}, 0, k_{P_3}, k_{P_4}, k_{P_5}, k_{P_6}\}$ and $\boldsymbol{K_D} = diag\{k_{D_1}, 0, k_{D_3}, k_{D_4}, k_{D_5}, k_{D_6}\}$, which have been experimentally optimized. To demonstrate the asymptotic convergence of the position error to zero, it is necessary to prove that $\boldsymbol{K_P^b}$ and $\boldsymbol{K_D^b}$ have strictly positive eigenvalues in the directions orthogonal to the puncture axis, i.e., the y-axis of the end-effector frame. This can be established by noting that $\boldsymbol{K_P^b} = \boldsymbol{A_d}^{-1}\boldsymbol{K_P}\boldsymbol{A_d}$ represents a similarity transformation, which preserves the eigenvalues of the original matrix $\boldsymbol{K_P}$. Since $\boldsymbol{K_P}$ has strictly positive eigenvalues in the directions orthogonal to the puncture axis, it can be concluded that, in those directions, the position error will asymptotically converge to zero. Additionally, to provide haptic feedback to the surgeon, the measured joint torque $\boldsymbol{\tau_s^{msr}}$ is used to derive forces/torques at the end effector through law of statics, which, based on the Novint Falcon model, are utilized to provide the surgeon with feedback on the forces/torques of interaction exchanged with the environment during the surgical procedure. Hence, the stabilizing action of the proposed parallel position/velocity control law is given by:

$$\boldsymbol{y} = \boldsymbol{J_A^\dagger}(\boldsymbol{q})\left[\boldsymbol{Ad^{-1}}\ (\boldsymbol{K_P}\ \boldsymbol{Ad}\ \tilde{\boldsymbol{x}} - \boldsymbol{K_D}\ \boldsymbol{Ad}\ \dot{\tilde{\boldsymbol{x}}} + \boldsymbol{K_F}\ F_R)\right] \quad (5)$$

where, in addition to the terms previously introduced, there is the term $\boldsymbol{K_F}F_R$. $\boldsymbol{K_F}$ is a 6×6 positive-define diagonal matrix defined as $\boldsymbol{K_F} = diag\{0, K_{F_2}, 0, 0, 0, 0\}$, and F_R is given by $F_R = k\ \tilde{v_s}$, where k is an experimentally chosen scaling factor, in order to have a limit on the force the robot applies, while $\tilde{v_s} = v_{y_s}^{des} - v_{y_s}^{msr}$ is the velocity error between the desired and measured needle insertion velocity.

b) OM2 - master-slave PEB mode: Similar to the parallel position/velocity control explained in the previous section, the master side employs a PD controller with high stiffness along the $\boldsymbol{x_m}$ and $\boldsymbol{z_m}$ axes. Conversely, as depicted in Fig. 3 for IOP2 with OM2, the slave side employs a master-slave PEB control, where the stabilizing action y is the same given by the Eq. 3. The key difference lies in the desired displacements along/around the axes of the slave frame. Specifically, the displacements along/around the $\boldsymbol{x_s}$ and $\boldsymbol{z_s}$ axes, relative to the initial state, are equal to zero thanks to the control applied on the master side. This configuration provides mechanical guidance to the surgeon during needle insertion, by restricting rotations and translations along the axes orthogonal to the puncture axis. In contrast, the desired displacement along the $\boldsymbol{y_s}$ axis is proportional to the displacement along the $\boldsymbol{y_m}$ axis, allowing for tracking of the Cartesian reference from the master side. In this operation mode, haptic feedback is provided to the surgeon, as well.

C. Experimental Setup

The experimental setup used to validate the proposed control strategy includes the components (shown in Fig. 4a):

- KUKA LWR 4+ (slave device): 7-degree-of-freedom (DOF) robotic arm with elastic joints [21], equipped with position and torque sensors at the joints. Communication between Kuka and a remote PC is provided by the ROS system with a 500-Hz UDP communication protocol. The transition between control modes is managed by a ROS package on the computer side, which utilizes the same functions from the Fast Robot Interface (FRI) library to load/unload control strategies and send commands to the KUKA Robot Controller (KRC), ensuring smooth transitions. Specifically, the transition occurs while the robot is stationary (initial state with zero velocity), guaranteeing stability during the control mode change.
- Novint Falcon (master device): a haptic interface that provides three DOF displacement sensing and force rendering. Its kinematics is a variant of the parallel delta-robot configuration. The workspace is characterized by a 3D displacement of $0.10\ [m]$ along each direction, and a maximum force feedback of about $9\ [N]$. It presents a handle with 4 buttons, which can be used to define various operation modes.
- Surgical tool: consists of a $0.27\ [m]$ long needle with a diameter of 14 gauge, which is able to pierce tissue and reach deep anatomical structures. To integrate the needle into the robot, a 3D-printed connection system was designed between the end effector and the surgical tool.
- Anatomical tissue model: a gelatin container replicating tissues the needle has to traverse to reach the kidney stone. The model (Fig. 4b) comprises two gelatin layers with different consistencies: a stiffer surface layer ($1 \times 10^{-4}\ [m]$) simulating the epidermis, and a softer deep layer ($0.08\ [m]$) representing the distance from target calyx to skin in ventral decubitus. A marker in the deep layer identifies the kidney stone target, while an obstacle represents anatomical structures to avoid during puncture.

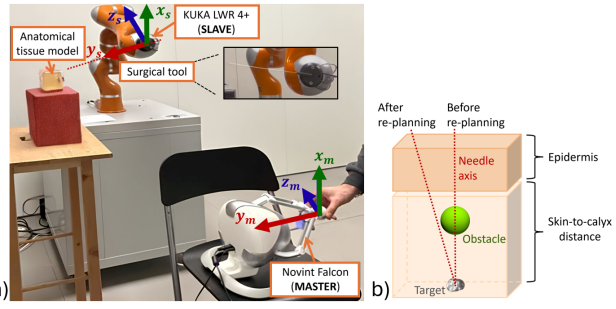

Fig. 4: a) Experimental setup, b) anatomical tissue model.

IEEE Robotics and Automation Letters (RA-L) paper, presented at ICRA 2026, Vienna, Austria. Cite as RA-L paper.

D. Experimental Protocol

a) Experimental Sessions: A group of six non-expert participants, composed of 2 males and 4 females, was recruited, with an average age of 24.67 ± 1.63. Each participant was required to operate the insertion of the needle into the anatomical model. It is important to note that during the experimental tests, the subjects directly observed the transparent anatomical model without the use of an imaging system, as the main goal was to assess how effectively the motion planner enabled the subjects to avoid obstacles while maintaining a safe distance. Moreover, the kidney stone position relative to the robotic system was considered known a priori, since numerous studies in literature have already demonstrated segmentation algorithms for target localization and spatial registration methods of the patient, robot, and imaging system into a common reference frame, using, for example, optoelectronic systems [22]. The target point displacement caused by the patient's breathing was not taken into account, as during the most critical phase, the patient is expected to remain in apnea.
Specifically, the test consisted of two consecutive phases. First, re-planning the access point using position control (Sect. II-B1): the robot started from a configuration that would collide with the obstacle, requiring the operator to re-plan the access point using Novint handle buttons for workspace scaling and recentering (Sect. II-B1). Second, advancing the needle along the puncture axis to reach the marker using OM1 (Sect. II-B2a) and OM2 (Sect. II-B2b). Each subject randomly performed five trials for each operation mode.

b) Performance Indices: The proposed control strategy has been evaluated in terms of i) intervention effectiveness, ii) intervention efficiency, and iii) system usability and acceptability. To evaluate the **intervention effectiveness**, the following four indices were considered (Eq. 6-9): Mean Deviation from the Needle Axis (*mean DNA*), Maximum Deviation from the Needle Axis (*max DNA*), Control Response Time (*CRT*) and Control Response Error (*CRE*). These metrics assess deviations from the desired puncture axis position/orientation and optimal insertion depth to reach the kidney stone, while quantifying system responsiveness to control commands. Therefore, the evaluation of effectiveness is based on puncture accuracy, a critical factor for surgical success. Angular deviation and offset relative to the final position are commonly used metrics for evaluating the accuracy of control strategies designed to align a surgical tool with both a desired trajectory and a target end position [23].

$$\textit{mean DNA} = \frac{1}{N}\sum_{i=1}^{N}\left|\arcsin\left(\frac{\boldsymbol{y}_{t_1}^{\mathbf{1}}\cdot\boldsymbol{y}_{t_1}^{i}}{\|\boldsymbol{y}_{t_1}^{\mathbf{1}}\|\cdot\|\boldsymbol{y}_{t_1}^{i}\|}\right)\right| \quad \text{[rad]} \tag{6}$$

$$\textit{max DNA} = \max_{i}\left\{\left|\arcsin\left(\frac{\boldsymbol{y}_{t_1}^{\mathbf{1}}\cdot\boldsymbol{y}_{t_1}^{i}}{\|\boldsymbol{y}_{t_1}^{\mathbf{1}}\|\cdot\|\boldsymbol{y}_{t_1}^{i}\|}\right)\right|\right\} \quad \text{[rad]} \tag{7}$$

where $\boldsymbol{y}_{t_1}^{\mathbf{1}}$ is the initial tool orientation along the puncture axis, and $\boldsymbol{y}_{t_1}^{i}$ is the tool orientation at the i-th instant.

$$\textit{CRT} = t_{\text{eff}} - t_{\text{des}} \quad \text{[s]} \tag{8}$$

where t_{des} represents the time at which the surgeon intends to stop the procedure, and t_{eff} represents the time at which the surgical tool actually stops.

$$\textit{CRE} = \int_{t_{\text{des}}}^{t_{\text{eff}}} v_m^S \,\mathrm{d}t \quad \text{[mm]} \tag{9}$$

where v_m^S represents the measured linear speed of the surgical tool. This metric allows quantifying the distance the tool travels during the delay caused by the control latency. To assess the **intervention efficiency**, the following two indices (Eq. 10-11) were considered: Needle Puncture Time (*NPT*), and Smoothness index (*SM*). The first one is the duration of needle puncture: a shorter time suggests fewer post-surgical complications and lower costs [18]. The second one is the movement smoothness: smoother movements typically suggest greater expertise and control, which can lead to fewer errors, less tissue damage, and a quicker recovery for the patient.

$$\textit{NPT} = t_{\text{fin}} - t_{\text{in}} \quad \text{[s]} \tag{10}$$

where t_{in} and t_{fin} represent the start and end times of the IOP2, respectively.

$$\textit{SM} = \frac{v_{mean}^S}{v_{max}^S} \tag{11}$$

where v_{mean}^S and v_{max}^S represent the mean and maximum measured linear speeds of the surgical tool, respectively. This speed-based metric has been validated as an effective measure of motion smoothness with high sensitivity and low within-group variability [24]. The **acceptability and usability** of the proposed strategy were evaluated through two different questionnaires. On the one hand, these questionnaires allow for the assessment of system usability, incorporating questions that gauge the ease of use and user confidence in utilizing the system. On the other hand, they facilitate the assessment of acceptability by exploring factors such as "Animacy", investigating the human-like and naturalness of interaction, and "Disturbance", analyzing whether subjects experience uncomfortable feelings and perceptions. The first questionnaire is the NASA Task Load Index (NASA-TLX), which is a multi-dimensional rating procedure providing an overall workload score based on a weighted average of ratings on six subscales: Mental Demands, Physical Demands, Temporal Demands, Own Performance, Effort, and Frustration. The NASA-TLX total score can assume values from 0 to 100, where higher values indicate a higher perceived workload. The second one includes the following questions: Q1) I felt in a comfortable position while performing the puncture, Q2) I did not feel tired (both physically and mentally) after the procedure, Q3) I did not feel my muscles fatigued after the procedure, Q4) The procedure did not require me to be very focused, Q5) I did not find the task difficult. Subjects' answers were quantified using a 5-point Likert scale (strongly agree = 5, strongly disagree = 1). Furthermore, urology residents were recruited to evaluate the proposed operation modes. The Likert questionnaire was extended with two additional questions specifically designed for expert evaluation: Q6) I think that the control strategy for performing needle insertion is intuitive, meaning it is easy to understand and adapt to, Q7) I think that the control

IEEE Robotics and Automation Letters (RA-L) paper, presented at ICRA 2026, Vienna, Austria. Cite as RA-L paper.

strategy is natural (not artificial), meaning it resembles the movement that a surgeon would perform manually during the traditional procedure. Finally, experts were asked to indicate their preference between OM1 and OM2.

c) Statistical Analysis: For each of the aforementioned indices, the mean and Standard Deviation (SD) were calculated, both across the five trials for each mode and for each subject, as well as across the total number of subjects for each operation mode. Finally, a Wilcoxon paired-sample analysis was conducted, as the Jarque-Bera test showed the data were not normally distributed.

III. RESULTS AND DISCUSSIONS

The results of the indices related to the evaluation of **procedure effectiveness and efficiency** obtained for the two operation modes are shown in Fig. 5. Regarding the accuracy of the two operation modes in maintaining the needle axis along the desired one, the results indicate that OM1 exhibits higher accuracy, with a max *DNA* in average equal to 0.006 ± 0.003 $[rad]$ ($p = 6 \cdot 10^{-6}$). Although the needle orientation in both operation modes is managed in the same way, the smoother movements allowed by OM1, as demonstrated below, likely contribute to this difference between the two operation modes, by reducing vibrations that could cause deviations in the needle tip orientation from the desired path. Notably, this result outperforms those reported for cooperative robot-aided percutaneous surgery, where the robot assists the surgeon by stabilizing the needle along the desired trajectory while the surgeon manually controls the end-effector (0.025 ± 0.024 $[rad]$), as well as AR-based visualization with robot guidance (0.019 ± 0.015 $[rad]$) [23]. As for the control responsiveness in terms of time, the graph in Fig. 5 indicates that OM2 achieves higher values of *CRT* than OM1, presenting a slower response to the stop command supplied by the surgeon. Nevertheless, the two operation modes do not exhibit a statistically significant difference, making them comparable. Overall, the results are positive, with a mean CRT of 0.47 ± 0.37 $[s]$ for OM2. Regarding the distance the needle travels from the moment the surgeon initiates the stop command until the needle actually stops, OM2 results to be more responsive, as there is a direct correspondence between the position command given by the surgeon from the master side and the movement of the needle from the slave side. On average, OM2 achieves a *CRE* equal to 0.8 ± 0.9 $[mm]$ ($p = 0.007$), which is comparable to the targeting error of 1.61 $[mm]$ reported for AR-based visualization with robot guidance and outperforms the 2.7 $[mm]$ achieved in cooperative robot-aided percutaneous surgery [23]. In terms of the time required for needle insertion, the two modes demonstrate comparable performance and significantly shorter *NPT* values compared to the manual technique with ultrasound guidance. Specifically, the median NPT values for OM1 and OM2 are 24.28 $[17.46, 35.84]$ $[s]$ and 26.00 $[22.06, 33.12]$ $[s]$, respectively. In contrast, the manual technique presents NPT values of 46.0 $[37.3, 96.8]$ $[s]$ [25]. Regarding *SM*, the graph in Fig. 5 clearly shows that OM1 exhibits a smoother trend, with an average SM of 0.13 ± 0.08 ($p = 0.005$). The higher

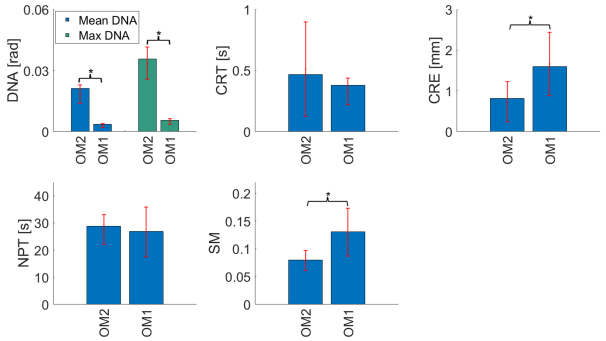

Fig. 5: Procedure effectiveness and efficiency indices. Red lines = 25–75th percentiles; curly brackets with * = $p < 0.05$.

TABLE I: Mean and SD of questionnaire scores

Questions	Non-experts		Experts	
	OM1	OM2	OM1	OM2
Q1	3.33 ± 0.57	3.33 ± 0.57	3.67 ± 1.03	2.83 ± 1.17
Q2	4.21 ± 0.41	4.21 ± 0.41	3.17 ± 1.17	3.33 ± 0.52
Q3	5	4.21 ± 0.41	3.83 ± 0.41	3.17 ± 1.17
Q4	4.21 ± 0.41	5	1.83 ± 0.41	2.17 ± 1.17
Q5	3.78 ± 0.87	3.33 ± 0.57	3.5 ± 0.82	3 ± 0.63
Q6	—	—	3.5 ± 0.55	3.33 ± 0.82
Q7	—	—	3.67 ± 0.82	3.5 ± 0.55
Likert	4.21 ± 0.41	4.69 ± 0.68	3.31 ± 0.68	3.05 ± 0.45
NASA	38.16 ± 5.93	31.19 ± 8.08	59.55 ± 9.17	56.83 ± 16.42

average value of SM associated with OM1 is likely attributed to the greater control over the velocity profile in this mode. Consequently, the velocity peaks deviate less from the average velocity. In contrast, OM2 lacks explicit control over the velocity profile, except for a limit on the maximum needle insertion velocity. Instead, the velocity assumes values that minimize the position error between the master and slave.

Finally, as for the **system usability and acceptability** evaluation, Table I presents the mean answers of Likert scale-based questions and the final scores of the two questionnaires. In the *Likert scale-based questionnaire*, no statistically significant difference was observed for any question in both expert and non-expert groups, indicating that the two operation modes were considered comparable in terms of comfort, physical and mental effort, and task ease. The scores for Q6 and Q7 show that experts consider both modes intuitive and similar to the traditional procedure. Overall, expert subjects gave slightly lower but still positive evaluations compared to non-experts, attributable to their greater familiarity with traditional procedures and heightened awareness of surgical complications. A particularly low score was obtained for Q4, indicating that experts believe high concentration is required, which could be mitigated through extended training. The final Likert score showed statistical significance ($p = 0.017$) for non-experts, favoring OM2, though the difference (0.48) remains negligible considering the scale ranging from 0 to 5. No statistical difference emerged for experts. For the *NASA-TLX* scores, no significant differences were found in either group, with OM2 showing slightly better scores. Expert subjects reported a moderately higher workload, aligning with previous observation. Based on their clinical experience, experts also confirmed the need for replanning functionality. Lastly, three of the six

expert participants expressed a preference for OM1, while the remaining three favored OM2. The results revealed that the two operation modes are comparable in terms of needle puncture time, and system usability and acceptability. However, they also have distinct advantages and disadvantages. OM1 allows for more accurate management of the desired needle orientation and offers greater smoothness of movement, while OM2 has proven to be more responsive, resulting in a smaller displacement error with respect to the intended end position. To leverage the advantages of both operation modes, a combined control strategy could be implemented. Specifically, until a certain distance from the area of interest, the OM1 - parallel position/velocity mode could be employed, allowing this first long tract to be traveled with great control over the desired needle orientation and smooth motion. It is important to note that, once the needle penetrates the tissue, adjustments to its orientation are no longer possible. Therefore, maximizing accuracy during the puncture is crucial. This is not always guaranteed for OM2 due to undesired vibrations. As the needle approaches the target, switching to OM2 - master-slave PEB mode would enhance accuracy in reaching the optimal insertion depth, thus ensuring that the needle stops exactly when the surgeon desires.

IV. CONCLUSION

This paper presents a tele-operated control strategy for minimally invasive percutaneous robotic surgery, demonstrated in a nephrolithotomy case. The system supports access-point re-planning via a cylindrical motion planner and position control, and provides two operation modes: OM1 (parallel position/velocity) and OM2 (master-slave PEB) for needle advancement. Six non-expert users evaluated the system in a simulated nephrolithotomy task on a synthetic model after training. The comparative analysis revealed distinct pros and cons for each mode. OM1 achieved higher orientation accuracy relative to the desired axis ($max\ DNA = 0.006 \pm 0.003\ [rad]$) and smoother motion ($SM = 0.13 \pm 0.08$), while OM2 responded better in terms of needle displacement from the target end position ($CRE = 0.8 \pm 0.9\ [mm]$). In other aspects, such as control response time, puncture time, usability, and acceptability, the two modes produced comparable results. Experts found both modes intuitive and consistent with traditional procedures, reporting moderate mental and physical workload. Experimental results also showed that the tele-operated approaches outperformed cooperative robotic systems in key metrics, likely due to improved dexterity from motion scaling. Both modes achieved performance comparable to, or better than, AR-based guidance, while maintaining lower system complexity. Future work will explore a combined control strategy enabling seamless switching between modes to exploit their respective strengths: OM1 for initial advancement to reduce angular deviation, and OM2 for high precision during the final approach. Further enhancements may include improved haptic feedback with tactile cues for tissue perception and integration of respiratory motion compensation to increase accuracy.

REFERENCES

[1] M. Uka *et al.*, "Magnetic resonance imaging guidance for percutaneous needle intervention," *Interv. Radiology*, 2023.

[2] N. Abolhassani *et al.*, "Needle insertion into soft tissue: A survey," *Medical Engineering & Physics*, vol. 29, no. 4, pp. 413–431, 2007.

[3] N. W. Jenkins *et al.*, "Intraoperative risks of radiation exposure for the surgeon and patient," *Annals of Translational Medicine*, vol. 9, 2020.

[4] K. Cheng *et al.*, "A systematic review of image-guided, surgical robot-assisted percutaneous puncture: Challenges and benefits," *Mathematical biosciences and engineering : MBE*, vol. 20, no. 5, p. 8375—8399, 2023.

[5] C. CN *et al.*, "Vision-based variable impedance control with oscillation observer for respiratory motion compensation during robotic needle insertion: a preliminary test," *The International Journal of Medical Robotics and Computer Assisted Surgery*, vol. 11, no. 4, pp. 502–511, 2015.

[6] S. Chen *et al.*, "Ultrasound-guided needle insertion robotic system for percutaneous puncture," *International Journal of Computer Assisted Radiology and Surgery*, 2021.

[7] E. Ben-David *et al.*, "Evaluation of a ct-guided robotic system for precise percutaneous needle insertion," *Journal of Vascular and Interventional Radiology*, 2018.

[8] G. Moustris *et al.*, "Evolution of autonomous and semi-autonomous robotic surgical systems: A review of the literature," *The international journal of medical robotics + computer assisted surgery : MRCAS*, vol. 7, 2011.

[9] M. Oo *et al.*, "Automated needle targeting with x-ray (ant-x) - robot-assisted device for percutaneous nephrolithotomy (pcnl) with its first successful use in human," *Journal of Endourology*, vol. 35, 2018.

[10] B. Guiu *et al.*, "Feasibility, safety and accuracy of a ct-guided robotic assistance for percutaneous needle placement in a swine liver model," *Scientific Reports*, vol. 11, 03 2021.

[11] L. Capodivento *et al.*, "A bidirectional human-machine control interface based on virtual fixtures for safe teleoperation of hyper-redundant robots," *IEEE Access*, 2024.

[12] M. Aggravi *et al.*, "Haptic teleoperation of flexible needles combining 3d ultrasound guidance and needle tip force feedback," *IEEE Robotics and Automation Letters*, 2021.

[13] M. Bernardes *et al.*, "Robot-assisted automatic insertion of steerable needles with closed-loop imaging feedback and intraoperative trajectory replanning," *Mechatronics*, vol. 23, no. 6, pp. 630–645, 2013.

[14] I. Kyriazis *et al.*, "Complications in percutaneous nephrolithotomy," *World Journal of Urology*, 2015.

[15] K. Taguchi *et al.*, "A randomized, single-blind clinical trial comparing robotic-assisted fluoroscopic-guided with ultrasound-guided renal access for percutaneous nephrolithotomy," *Journal of Urology*, vol. 208, 05 2022.

[16] I. Masarwe *et al.*, "Querying the significance of patient position during computerized tomography on the reliability of pre-percutaneous nephrolithotomy planning," *World Journal of Urology*, vol. 40, pp. 1–8, 06 2022.

[17] A. Deshmukh *et al.*, "Renal displacement with supine to prone positional change: Effect of sex and bmi," *Journal of Endourology*, vol. 36, 07 2021.

[18] O. Babayoff *et al.*, "Surgery duration: Optimized prediction and causality analysis," *PLoS ONE*, vol. 17, 2022.

[19] B. Siciliano *et al.*, *Robotics: Modelling, Planning and Control*. London: Springer, 2009.

[20] C. Lauretti *et al.*, "A surgeon-robot shared control for ergonomic pedicle screw fixation," *IEEE Robotics and Automation Letters*, vol. 5, no. 2, pp. 2554–2561, 2020.

[21] L. Zollo *et al.*, "Regulation with on-line gravity compensation for robots with elastic joints," in *IEEE International Conference on Robotics and Automation, 2004. Proceedings. ICRA '04. 2004*, vol. 3, 2004, pp. 2687–2692 Vol.3.

[22] G. Dagnino *et al.*, "Intra-operative fiducial-based ct/fluoroscope image registration framework for image-guided robot-assisted joint fracture surgery," *International Journal of Computer Assisted Radiology and Surgery*, 2017.

[23] J. Fu *et al.*, "Augmented reality and human–robot collaboration framework for percutaneous nephrolithotomy: System design, implementation, and performance metrics," *IEEE Robotics Automation Magazine*, 2024.

[24] P. Gulde *et al.*, "Smoothness metrics in complex movement tasks," *Frontiers in Neurology*, vol. 9, p. 615, 09 2018.

[25] K. Taguchi *et al.*, "Robot-assisted fluoroscopy- vs ultrasound-guided renal access for nephrolithotomy: A phantom model bench-top study," *Journal of Endourology*, vol. 33, 10 2019.